







RESEARCH ARTICLE | APRIL 23 2024

# Dissipation-induced collective advantage of a quantum thermal machine **FREE**

Special Collection: [Quantum Systems Far From Equilibrium](#)

Matteo Carrega ; Luca Razzoli ; Paolo Andrea Erdman ; Fabio Cavaliere ; Giuliano Benenti ; Maura Sasseti 



AVS *Quantum Sci.* 6, 025001 (2024)

<https://doi.org/10.1116/5.0190340>



# Dissipation-induced collective advantage of a quantum thermal machine

Cite as: AVS Quantum Sci. 6, 025001 (2024); doi: 10.1116/5.0190340

Submitted: 5 December 2023 · Accepted: 2 April 2024 ·

Published Online: 23 April 2024



View Online



Export Citation



CrossMark

Matteo Carrega,<sup>1,a)</sup> Luca Razzoli,<sup>2,3</sup> Paolo Andrea Erdman,<sup>4</sup> Fabio Cavaliere,<sup>1,5</sup> Giuliano Benenti,<sup>2,3,6</sup> and Maura Sassetti<sup>1,5</sup>

## AFFILIATIONS

<sup>1</sup>CNR-SPIN, Via Dodecaneso 33, 16146 Genova, Italy

<sup>2</sup>Center for Nonlinear and Complex Systems, Dipartimento di Scienza e Alta Tecnologia, Università degli Studi dell'Insubria, Via Valleggio 11, 22100 Como, Italy

<sup>3</sup>Istituto Nazionale di Fisica Nucleare, Sezione di Milano, Via Celoria 16, 20133 Milano, Italy

<sup>4</sup>Department of Mathematics and Computer Science, Freie Universität Berlin, Arnimallee 6, 14195 Berlin, Germany

<sup>5</sup>Dipartimento di Fisica, Università di Genova, Via Dodecaneso 33, 16146 Genova, Italy

<sup>6</sup>NEST, Istituto Nanoscienze-CNR, Piazza San Silvestro 12, I-56127 Pisa, Italy

**Note:** This paper is part of the special issue on Quantum Systems Far From Equilibrium.

<sup>a)</sup> Author to whom correspondence should be addressed: [matteo.carrega@spin.cnr.it](mailto:matteo.carrega@spin.cnr.it)

## ABSTRACT

Do quantum correlations lead to better performance with respect to several different systems working independently? For quantum thermal machines, the question is whether a working medium (WM) made of  $N$  constituents exhibits better performance than  $N$  independent engines working in parallel. Here, by inspecting a microscopic model with the WM composed by two non-interacting quantum harmonic oscillators, we show that the presence of a common environment can mediate non-trivial correlations in the WM leading to better quantum heat engine performance—maximum power and efficiency—with respect to an independent configuration. Furthermore, this advantage is striking for strong dissipation, a regime in which two independent engines cannot deliver any useful power. Our results show that dissipation can be exploited as a useful resource for quantum thermal engines and are then corroborated by optimization techniques here extended to non-Markovian quantum heat engines.

Published under an exclusive license by AIP Publishing. <https://doi.org/10.1116/5.0190340>

## I. INTRODUCTION

On the road to the development of quantum technologies,<sup>1</sup> a fundamental question is whether quantum correlations between the constituents of a system can improve performances.<sup>2</sup> (for instance, the qubits in a quantum computer). In the context of quantum thermal machines,<sup>3–20</sup> the question can be posed as follows: can a working medium (WM) made of  $N$  constituents show better performances than  $N$  independent engines working in parallel? Furthermore, can unavoidable dissipation be exploited to improve machine performance or does it only play a detrimental role? Even though previous investigations remarkably found parameter regions where a positive answer,<sup>21–34</sup> even related to damping induced phenomena<sup>35–46</sup> can be given, a complete picture has not yet been achieved. In this work, we show that a quantum heat engine where the working medium is composed by two non-interacting quantum harmonic oscillators (QHOs),

connected to common baths—see Fig. 1(a)—via periodically modulated couplings,<sup>47–49</sup> exhibits an improvement in performance due to bath-mediated correlations<sup>35,37</sup> with respect to the case of two independent single-oscillator engines working in parallel—see Fig. 1(b). This effect is striking in the case of strong dissipation, when one would naively expect overdamped dynamics and poor performance of the engine. While this is the case for independent machines, for which the engine operating regime disappears, the presence of common baths sustains instead efficiency and power of the engine. We explain this surprising result in terms of the appearance, at strong damping, of a frequency- and phase-locked mode,<sup>50–53</sup> in which the oscillators have a common frequency and oscillate in phase opposition. This normal mode turns out to be only weakly damped, with a damping time increasing with the dissipation strength. Our results are first illustrated in the case of monochromatic drives, and then corroborated

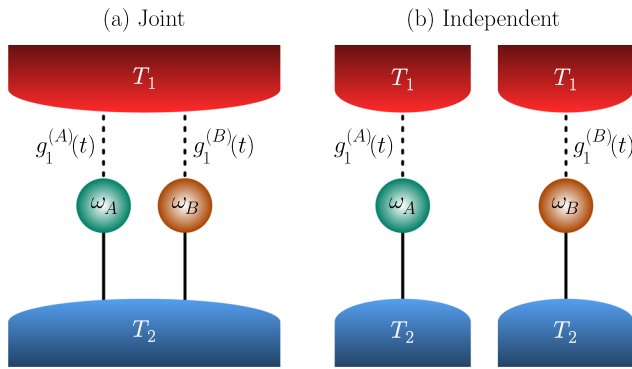


**Fig. 1.** Sketch of the dynamical quantum heat engines under study. The external driving of the machine occurs through *generic* periodic modulations of the couplings with one reservoir. (a) Two quantum harmonic oscillators, with frequencies  $\omega_A$  and  $\omega_B$ , are in contact with two common thermal reservoirs at temperatures  $T_\nu$ , with  $\nu = 1, 2$ . The WM exchanges heat currents  $J_\nu$  with the reservoirs and total power  $P$  generated by an external drive that periodically modulates the weak coupling with the  $\nu = 1$  reservoir (dashed lines). The  $\nu = 2$  WM-bath coupling is static and much stronger (solid lines). (b) Two uncoupled oscillators in the same configuration as in panel (a) but now in contact with independent thermal reservoirs. Here, no correlations are mediated by the baths, and the quantum thermal machine consists of independent two-terminal devices working in parallel.

optimizing over arbitrary periodic drivings by means of a gradient optimization methods (a technique at the heart of many machine learning problems<sup>54–61</sup>), without any *a priori* assumption on the shape or speed of the drivings. Furthermore, we characterize the heat engine performance in terms of both efficiency and extracted power. These quantities cannot be simultaneously optimized: indeed, high power engines typically exhibit a low efficiency, and vice versa. We, thus, employ the concept of the Pareto front,<sup>62</sup> recently employed in the context of quantum thermodynamics,<sup>54,57,58,63–65</sup> to find optimal tradeoffs between the power and the efficiency of the engine. Our calculations of the Pareto front extend the optimization approach to non-Markovian quantum thermodynamics, beyond the standard Lindblad approximation. Finally, we have investigated whether there is a relationship between collective advantage and the establishment of non-classical correlations between the two quantum harmonic oscillators (QHOs), focusing on the logarithmic negativity<sup>37,66–71</sup> as a measure of entanglement. While we could not find a direct connection between entanglement and collective advantage, we obtained as an interesting by-product a protocol to measure entanglement via a small number of measurements of thermodynamic quantities, more precisely of the output work at specific operating conditions, instead of a full quantum tomography to reconstruct the density matrix of the system.

## II. GENERAL SETTING AND THERMODYNAMIC OBSERVABLES

### A. Model

We consider a quantum thermal machine, where the WM is in contact with two thermal reservoirs  $\nu = 1, 2$ , respectively, at temperatures  $T_1$  and  $T_2$ . The WM is composed of two uncoupled (no direct coupling) QHOs, labeled  $l = A, B$ , as sketched in Fig. 1(a). This configuration with common environments, dubbed *joint*, will be compared with the one sketched in Fig. 1(b), where two independent QHOs work in parallel with separate baths. The WM-bath couplings

with the  $\nu = 1$  reservoir are assumed weak and governed by a time-dependent periodic modulation<sup>47–49</sup>  $g_1^{(l)}(t) = g_1^{(l)}(t + T)$  with period  $T = 2\pi/\Omega$ . On the other hand, the couplings with the  $\nu = 2$  reservoir are static,  $g_2^{(l)} = 1$ . Coupling modulation can be suitably engineered to perform thermodynamic tasks,<sup>47–49</sup> and here, we shall focus on the heat engine working mode.

The total Hamiltonian is (we set  $\hbar = k_B = 1$ )<sup>72</sup>

$$H^{(t)} = \sum_{l=A,B} H_l + \sum_{\nu=1,2} [H_\nu + H_{\text{int},\nu}^{(t)}], \quad (1)$$

where the Hamiltonian of the  $l$ th QHO reads  $H_l = (p_l^2/2m) + (1/2)m\omega_l^2 x_l^2$ , with the two QHOs having different characteristic frequencies  $\omega_A$  and  $\omega_B$ . The reservoirs are modeled in the Caldeira–Leggett framework<sup>73–76</sup> as a collection of independent harmonic oscillators

$$H_\nu = \sum_{k=1}^{+\infty} \left( \frac{p_{k,\nu}^2}{2m_{k,\nu}} + \frac{1}{2} m_{k,\nu} \omega_{k,\nu}^2 X_{k,\nu}^2 \right). \quad (2)$$

A bilinear coupling in the WM and bath position operators, weighted by the driving controls  $g_\nu^{(l)}(t)$ , describes the WM–reservoir interactions

$$H_{\text{int},\nu}^{(t)} = \sum_{l=A,B} \sum_{k=1}^{+\infty} \left[ -g_\nu^{(l)}(t) c_{k,\nu}^{(l)} x_l X_{k,\nu} + \frac{(g_\nu^{(l)}(t) c_{k,\nu}^{(l)})^2}{2m_{k,\nu} \omega_{k,\nu}^2} x_l^2 + \frac{g_\nu^{(l)}(t) g_\nu^{(\bar{l})}(t) c_{k,\nu}^{(l)} c_{k,\nu}^{(\bar{l})}}{2m_{k,\nu} \omega_{k,\nu}^2} x_l x_{\bar{l}} \right], \quad (3)$$

where we introduced the convention according to which if  $l = A$  then  $\bar{l} = B$ , and vice versa. The factors  $c_{k,\nu}^{(l)}$  represent the coupling between the  $l$ th QHO and the  $k$ th mode of the  $\nu$ th reservoir. In the following, we assume that the couplings with the bath  $\nu = 2$  are much stronger than those with the bath  $\nu = 1$ . Without loss of generality, we also choose for the bath  $\nu$  equal couplings  $c_{k,\nu}^{(A)} = c_{k,\nu}^{(B)} \equiv c_{k,\nu}$ . Looking at the coupling with the static bath  $\nu = 2$ , this choice of equal couplings leads to a mirror symmetry  $A \leftrightarrow B$ . In the resonant case  $\omega_A = \omega_B$ , this symmetry explains the existence of a dissipation-free subspace, with the normal mode corresponding to relative coordinate  $x_A - x_B$  completely undamped.<sup>35,37,38</sup> However, this implies that in the resonant case, the system cannot reach a periodic steady state, and thus, we are not going to deal with this case in the rest of this work. The interaction in Eq. (3) includes counter-term contributions that serve two purposes: to avoid renormalizations of the characteristic frequencies of the QHOs  $\omega_{A,B}$  and to cancel the direct coupling among them, which would naturally arise in the Caldeira–Leggett model (see the supplementary material). The properties of the bath  $\nu$  are governed by the so-called spectral density<sup>74</sup>

$$\mathcal{J}_\nu(\omega) \equiv \frac{\pi}{2} \sum_{k=1}^{+\infty} \frac{c_{k,\nu}^2}{m_{k,\nu} \omega_{k,\nu}} \delta(\omega - \omega_{k,\nu}). \quad (4)$$

Finally, we assume that at initial time  $t_0 \rightarrow -\infty$ , the reservoirs are in their thermal equilibrium at temperatures  $T_\nu$ , with the total density matrix written in a factorized form  $\rho(t_0) = \rho_A(t_0) \otimes \rho_B(t_0) \otimes \rho_1(t_0) \otimes \rho_2(t_0)$ , where  $\rho_l(t_0)$  is the initial density matrix of each

QHO ( $l = A, B$ ), and  $\rho_\nu(t_0) = \exp(-H_\nu/T_\nu)/\text{Tr}[\exp(-H_\nu/T_\nu)]$  is the thermal density matrix of each reservoir ( $\nu = 1, 2$ ).

### B. Thermodynamic quantities

Hereafter, we work in the Heisenberg picture, and we focus on averaged thermodynamic quantities such as power and heat currents, which determine the working regime and the performance of a quantum thermal machine. Except in the resonant case  $\omega_A \equiv \omega_B$ ,<sup>35,37</sup> due to dissipation, the WM reaches a periodic steady state regardless of the initial conditions. We then concentrate on quantities averaged over the period  $T$ , in the off resonant case  $\omega_B < \omega_A$ . The average power is defined as

$$P \equiv \int_0^T \frac{dt}{T} \langle P(t) \rangle = \int_0^T \frac{dt}{T} \text{Tr} \left[ \frac{\partial H_{\text{int},1}(t)}{\partial t} \rho(t_0) \right], \quad (5)$$

where we have introduced both the temporal and quantum averages (the latter denoted by  $\langle \dots \rangle$ ),  $t_0 \rightarrow -\infty$  is the initial time, and  $\rho(t_0)$  the initial density matrix of the system (see Appendix A). Notice that a working heat engine is obtained when  $P < 0$ . Similarly, the average heat current associated with the  $\nu$ th reservoir reads

$$J_\nu \equiv \int_0^T \frac{dt}{T} \langle J_\nu(t) \rangle = - \int_0^T \frac{dt}{T} \text{Tr} [\dot{H}_\nu(t) \rho(t_0)] \quad (6)$$

with  $J_\nu > 0$  when energy flows into the WM. The average power and heat currents are expressed (see Appendix A) in terms of the QHOs and bath position operators  $x_l(t)$  and  $X_{k,\nu}(t)$ , respectively. The exact solution for  $X_{k,\nu}(t)$  can be found by inspecting the set of coupled equations of motion, see also the supplementary material. The behavior of thermodynamic quantities is eventually determined by the dynamics of  $x_A(t)$  and  $x_B(t)$ .

As discussed in Ref. 48, the aforementioned quantities satisfy the energy balance relation  $P + \sum_\nu J_\nu = 0$ , in compliance with the first law of thermodynamics. Another relevant quantity of interest is the so-called entropy production rate  $\sigma \equiv -\sum_\nu J_\nu/T_\nu$ . In accordance with the second law of thermodynamics, it is always<sup>10,77</sup>  $\sigma \geq 0$ . This represents another key figure of merit for thermal machines: for instance, for a good heat engine, one should look for the best power output while minimizing at the same time the entropy production rate.

## III. RESULTS

### A. Bath-induced dynamics and response functions

Under the assumption that the WM is weakly coupled to the modulated  $\nu = 1$  reservoir, a perturbative approach in  $H_{\text{int},1}^{(t)}$  is considered. The final expressions for the average power and heat current read (see the supplementary material)

$$P = - \sum_{n=-\infty}^{+\infty} n\Omega \int_{-\infty}^{+\infty} \frac{d\omega}{2\pi m} \mathcal{J}_1(\omega + n\Omega) N(\omega, n\Omega) \mathbf{g}_n^\dagger \cdot \chi_2''(\omega) \cdot \mathbf{g}_n \quad (7)$$

and

$$J_1 = \sum_{n=-\infty}^{+\infty} \int_{-\infty}^{+\infty} \frac{d\omega}{2\pi m} (\omega + n\Omega) \mathcal{J}_1(\omega + n\Omega) N(\omega, n\Omega) \mathbf{g}_n^\dagger \cdot \chi_2''(\omega) \cdot \mathbf{g}_n, \quad (8)$$

and  $J_2 = -(P + J_1)$ . In the above expressions enter  $\mathcal{J}_1(\omega)$ , the spectral density of the  $\nu = 1$  bath, governing memory effects, and the function

$$N(\omega, \Omega) = \coth\left(\frac{\omega + \Omega}{2T_1}\right) - \coth\left(\frac{\omega}{2T_2}\right). \quad (9)$$

It is worth noticing that the aforementioned quantities are written as quadratic forms where we have introduced the  $2n$  components vector  $\mathbf{g}_n = (g_n^{(A)}, g_n^{(B)})^t$  (and  $\mathbf{g}_n^\dagger$  its adjoint) with  $g_n^{(l)}$  the  $n$ th Fourier coefficient of  $g_1^{(l)}(t)$ . We assume that these coefficients are related to two independent drive sources, and hence, they satisfy two independent constraints

$$\sum_n |g_n^{(l)}|^2 = g^{(l)2}, \quad \text{for } l = A, B, \quad (10)$$

where  $g^{(l)}$  are two fixed normalization constants. Both  $P$  and  $J_\nu$  depend on the imaginary part,  $\chi_2''(\omega)$ , of the retarded response matrix  $\chi_2(\omega) = \chi_2'(\omega) + i\chi_2''(\omega)$ . The elements of the two-by-two matrix are indeed the Fourier transform of  $(l, l' = A, B)$

$$\chi_2^{(l,l')}(t) \equiv im\theta(t) \left\langle \left[ x_l^{(0)}(t), x_{l'}^{(0)}(0) \right] \right\rangle, \quad (11)$$

where  $\theta(t)$  is the step function and  $x_l^{(0)}(t)$  evolve under the unperturbed Hamiltonian and their response functions are linked to the static  $\nu = 2$  bath only (see Appendix B). Their imaginary parts read

$$\begin{aligned} \chi_2^{(ll)''}(\omega) &= \frac{\omega(\omega^2 - \omega_l^2)^2 \gamma_2'(\omega)}{|D(\omega)|^2}, \\ \chi_2^{(ll')''}(\omega) &= \frac{\omega(\omega^2 - \omega_l^2)(\omega^2 - \omega_{l'}^2) \gamma_2'(\omega)}{|D(\omega)|^2}, \end{aligned} \quad (12)$$

$$D(\omega) = (\omega^2 - \omega_A^2)(\omega^2 - \omega_B^2) + i\omega(2\omega^2 - \omega_A^2 - \omega_B^2)\gamma_2(\omega), \quad (13)$$

where  $\gamma_2'(\omega)$  is the real part of the damping kernel  $\gamma_2(\omega)$  of the bath  $\nu = 2$  (see Appendix B). In the following discussion, we will assume a Ohmic spectral density for the latter bath, which implies  $\gamma_2(\omega) = \gamma_2$ , a constant real number.<sup>74</sup> Looking at the structure of the symmetric matrix  $\chi_2''(\omega)$ , one can notice that at any frequency  $\omega$ , there is a null eigenvalue and a finite one given by

$$\lambda = \frac{\gamma_2 \omega}{|D(\omega)|^2} [2\omega^4 - 2(\omega_A^2 + \omega_B^2)\omega^2 + \omega_A^4 + \omega_B^4]. \quad (14)$$

It turns out that its associated frequency-dependent eigenvector, when evaluated at  $\omega_{A/B}$  corresponds to the *localized* vector  $(1, 0)^t / (0, 1)^t$ . Furthermore, it is possible to find a completely *delocalized* and anti-symmetric eigenvector  $(-1, 1)^t$ . This is achieved when the frequency is equal to

$$\bar{\omega} = \sqrt{\frac{\omega_A^2 + \omega_B^2}{2}}, \quad (15)$$

whose value will play an important role (see below). It is instructive to evaluate the imaginary part of the response function at these three points:

$$\chi_2''(\omega_l) = \frac{1}{\gamma_2 \omega_l} \begin{pmatrix} \delta_{l,A} & 0 \\ 0 & \delta_{l,B} \end{pmatrix} \quad (16)$$

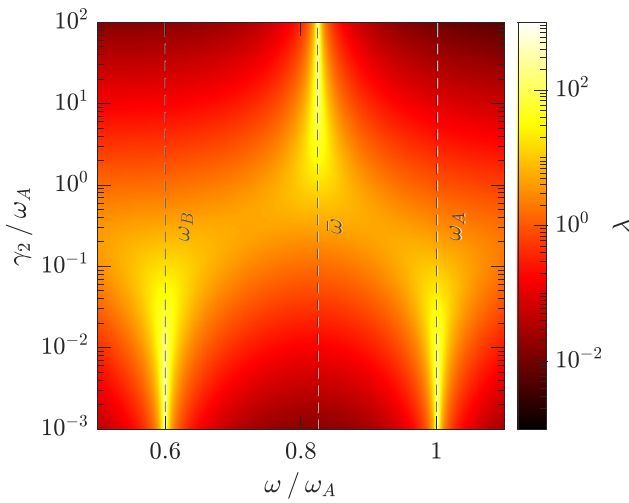


**Fig. 2.** Density plot of the eigenvalue  $\lambda$  as a function of frequency  $\omega$  and damping strength  $\gamma_2$  (in units of  $\omega_A$ ). We have fixed  $\omega_A = 1$  and  $\omega_B = 0.6$ . Notice that with this choice  $\bar{\omega}$  of Eq. (15) corresponds to 0.82.

and

$$\chi_2''(\bar{\omega}) = \frac{\gamma_2 \bar{\omega}}{\Delta^4} \begin{pmatrix} 1 & -1 \\ -1 & 1 \end{pmatrix}, \quad (17)$$

where we introduced  $\Delta = \sqrt{(\omega_A^2 - \omega_B^2)/2}$  for notational convenience. From the above expression, a completely different behavior as a function of  $\gamma_2$  emerges. Indeed, for  $\gamma_2 \ll \omega_l$ , the localized modes are predominant, while they subside for  $\gamma_2 \gg \omega_l$ , when the delocalized mode becomes the leading one, as can be seen by the prefactors of the above matrices. In Fig. 2, we plot the finite eigenvalue  $\lambda$  in a density plot as a function of frequency  $\omega$  and damping strength  $\gamma_2$ . From this picture the above structure, and its evolution with increasing damping strength, becomes clear.

This shows that the system response crucially depends on the damping strength  $\gamma_2$ . More precisely, this can be seen by inspecting the zeros of  $D(\omega)$  that govern intrinsic excitations of the normal modes (see also Appendix B). Explicitly, at very weak damping (i.e., when  $\gamma_2 \ll \omega_l$ )  $\chi_2''(\omega)$  resembles the one of two independent QHOs with differences of order  $O(\gamma_2/\omega_l)$ . Conversely, in the opposite strong damping regime (i.e., when  $\gamma_2 \gg \Delta^4/\bar{\omega}^3$ ), the key result is that the WM becomes effectively *frequency locked* to a unique characteristic frequency. In this regime, the two QHOs oscillate, at finite time, with a common frequency  $\bar{\omega}$ . Moreover, they are also *phase locked* in anti-phase (see Appendix B). This important behavior is tightly related to *bath-mediated correlations*: indeed,  $\gamma_2$  plays a twofold role. On the one hand, it is responsible for dissipation but, on the other hand, it also mediates an effective coupling between the two QHOs, establishing non-trivial correlations between them even without any direct, *a priori* coupling.

## B. Quantum thermal machine performance

We now present the effect of bath-mediated correlations on the performance of a dynamical heat engine. To ensure a working heat

engine,<sup>48,49</sup> we choose for the bath  $\nu = 1$  a structured non-Markovian environment<sup>78–83</sup> with a Lorentzian spectral function

$$\mathcal{J}_1(\omega) = \frac{d_1 m \gamma_1 \omega}{(\omega^2 - \omega_1^2)^2 + \gamma_1^2 \omega^2} \quad (18)$$

with a peak centered at  $\omega \sim \omega_1$ , an amplitude governed by  $d_1$ , and a width determined by  $\gamma_1$ . Notice that for sufficiently small  $\gamma_1$ , this spectral density acts as a sharp filter, centered around  $\pm \omega_1$ . Such structured environment represents a common example of non-Markovian bath<sup>48,81</sup> and can be realized with state-of-the-art superconducting circuits.<sup>84–87</sup>

To begin, we investigate the output power produced by the heat engine, in the simple case of a monochromatic drive:  $g_1^{(A)}(t) = \cos(\Omega t)$  and  $g_1^{(B)}(t) = \cos(\Omega t + \phi)$ , with  $\Omega$  the external frequency and  $\phi$  the relative phase of two independent drives. Although the choice of a single harmonic might seem a simplifying assumption, below we show that in most cases this represents the optimal one. In this case, in order to enforce the two constraints in Eq. (10) with the symmetric choice  $g^{(l)} = 1/\sqrt{2}$ , one has  $g_n^{(A)} = \delta_{n,\pm 1}/2$  and  $g_n^{(B)} = e^{\mp i\phi} \delta_{n,\pm 1}/2$  and Eq. (7) becomes

$$P = -\Omega \int_{-\infty}^{+\infty} \frac{d\omega}{4\pi m} \mathcal{J}_1(\omega + \Omega) N(\omega, \Omega) \chi_{\text{eff}}''(\omega) \quad (19)$$

with

$$\chi_{\text{eff}}(\omega) = \chi_2^{(A,A)}(\omega) + \chi_2^{(B,B)}(\omega) + 2 \cos(\phi) \chi_2^{(A,B)}(\omega), \quad (20)$$

an effective response function that explicitly depends on the phase  $\phi$ , governing the constructive/destructive interference induced by the non-diagonal term  $\chi_2^{(A,B)}$ . Looking for the maximum output power, with these two monochromatic drives, it is easy to see that only two phase values are relevant, i.e.,  $\phi = 0$  or  $\phi = \pi$ . Indeed, for  $\phi = 0$ ,  $\chi_{\text{eff}}''(\omega)$  is peaked around  $\omega \sim \omega_l$ , while for  $\phi = \pi$  it is peaked around  $\omega \sim \bar{\omega}$ .

To appreciate the effects of bath-mediated correlations, the output power produced by the joint configuration of Fig. 1(a) should be compared to the one obtained in the independent configuration of Fig. 1(b). In the latter case,  $P$  is given by an expression analogous to Eq. (19) where  $\chi_{\text{eff}}(\omega) \rightarrow \chi_{\text{eff,ind}}(\omega) = -\sum_{l=A,B} (\omega^2 - \omega_l^2 + i\gamma_2 \omega)^{-1}$ .

In the limit of small damping strength  $\gamma_2 \rightarrow 0$ , the response function  $\chi_2(\omega)$  reduces to the one above, and therefore, no collective effects are expected to show up. However, we know that the response functions qualitatively change while increasing the damping strength. To see these effects in Fig. 3(a), we consider the case of a moderate damping strength  $\gamma_2 = 0.1\omega_A$ . Here, the engine output power is reported considering the temperature configuration<sup>88</sup>  $T_1 = 0.6\omega_A$ ,  $T_2 = 0.4\omega_A$ , and the representative value  $\omega_B = 0.6\omega_A$ . The density plot in the  $\omega_1 - \Omega$  plane shows the working regions of the dynamical heat engine, where  $P < 0$ . From the figure, it is clear that these regions follow two distinct sectors that correspond to the lines  $\omega_1 = \omega_l + \Omega$  with  $l = A, B$ . This is due to the Lorentzian spectral density of Eq. (18) acting as an effective filter. For the representative value  $\omega_B = 0.6\omega_A$ , the maximum output power is obtained for  $\phi = 0$ . Already at this moderate damping  $\gamma_2 = 0.1\omega_A$ , a dissipation-induced benefit in the output power starts to emerge. This can be seen looking at the smaller values in the inset of Fig. 3(a), where the power of the independent case of Fig. 1(b) is reported.

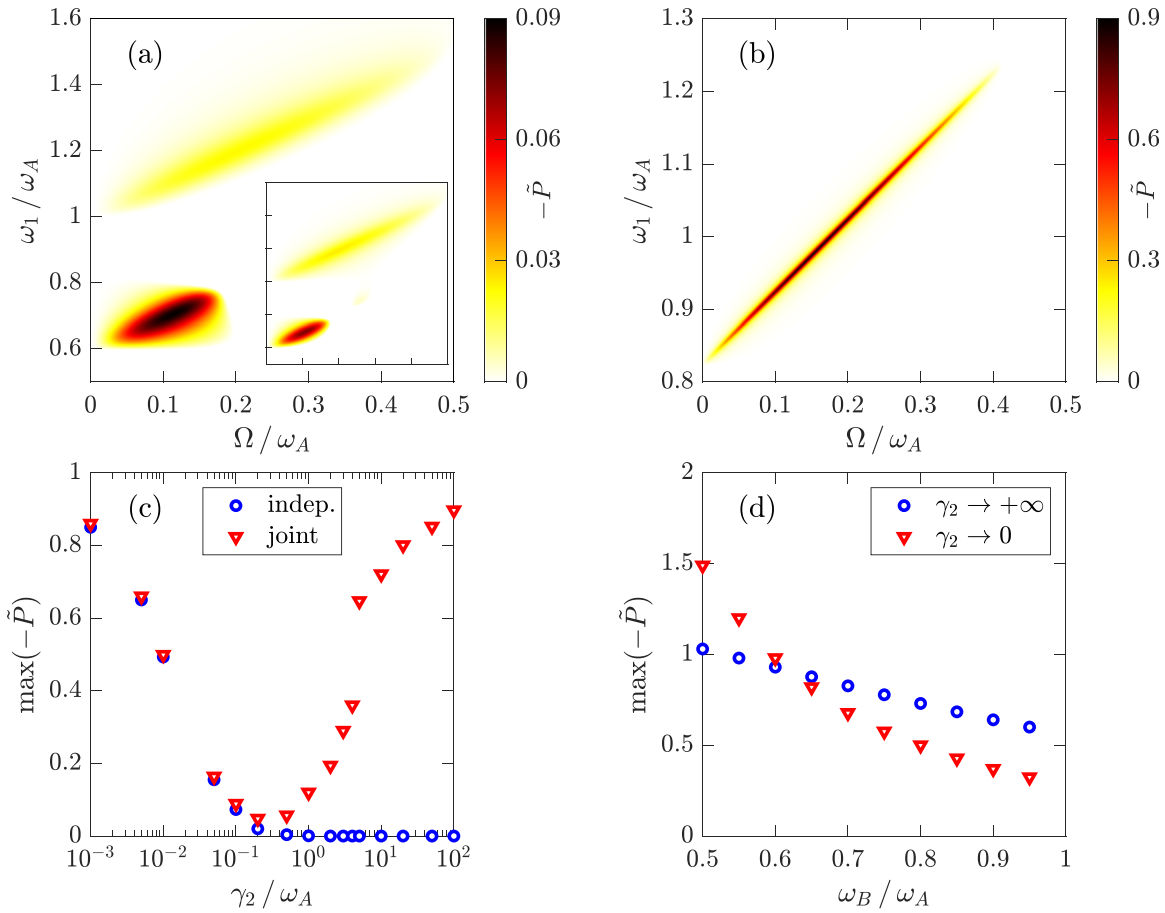


**FIG. 3.** Output power of Eq. (19) for the dynamical heat engine with a monochromatic drive. (a) Density plot of the (dimensionless) output power  $-\bar{P} = -P\omega_A^2/d_1$  for the joint configuration, obtained by optimizing with respect to the phase displacement  $\phi$ , as a function of  $\Omega/\omega_A$  and  $\omega_1/\omega_A$  with  $\omega_B = 0.6\omega_A$ ,  $\phi = 0$ , and damping strength  $\gamma_2 = 0.1\omega_A$ . The inset shows the comparison with the independent configuration of Fig. 1(b), on the same scale. (b) Same as in panel (a) but for strong dissipation with  $\gamma_2 = 100\omega_A$  and  $\phi = \pi$  (see the text). (c) Maximum output power for the representative value  $\omega_B = 0.6\omega_A$  as a function of damping strength  $\gamma_2$ , both in the joint and in the independent case. For the joint case, power is maximized over  $\omega_1$ ,  $\Omega$ , and  $\phi$ . (d) Maximum output power for the joint configuration in the very weak ( $\gamma_2 \rightarrow 0$ ) and ultra-strong ( $\gamma_2 \rightarrow \infty$ ) regime, as a function of  $\omega_B/\omega_A$ . Here, the same optimization as in panel (c) has been performed. Other parameters are:  $T_1 = 0.6\omega_A$ ,  $T_2 = 0.4\omega_A$ , and  $\gamma_1 = 0.01\omega_A$ .

Marked signatures of bath-mediated correlations shows up in the strong dissipation regime ( $\gamma_2 \gg \omega_{A,B}$ ), when full frequency locking is established, as reported in Fig. 3(b) with  $\gamma_2 = 100\omega_A$ . Strikingly, the joint configuration results in a wide and sizeable working regime for the dynamical heat engine. Moreover, differently from panel (a), the working region is now concentrated along a single line, i.e.,  $\omega_1 = \bar{\omega} + \Omega$  that extends over a wider region in the  $\omega_1 - \Omega$  plane. The fact that only a single region now appears is consistent with the frequency locking mechanism, with the maximum power obtained for  $\phi = \pi$ . In addition, comparing the moderate and strong damping situation, one can note a large increase in the output power magnitude observed for this parameter choice. The behavior of the power as a function of the damping strength  $\gamma_2$ , both for the joint and the independent configuration, is analyzed in Fig. 3(c), where the maximum output power is reported. It is clear that above a certain critical value of  $\gamma_2$  the independent configuration is fully overdamped and ceases to work as a heat engine, while on the contrary, the joint configuration

exhibits a solid and stable performance. Finally, in Fig. 3(d), we have reported the maximum output power of the joint case for the two opposite regimes of very weak ( $\gamma_2 \rightarrow 0$ ) and ultra-strong ( $\gamma_2 \rightarrow \infty$ ) damping, whose behaviors can be obtained in analytic form (see Appendix C). In the former, weak damping regime, one finds a phase-independent, completely uncorrelated power. In the latter, instead,  $\gamma_2 \rightarrow \infty$  regime, the dependence on the phase  $\phi$  is crucial: only for  $\phi = \pi$  one obtains  $P < 0$ . Figure 3(d) shows that a wide region of parameters exists where the strong dissipation regime can even outperform over its weak counterpart, demonstrating that frequency locking can be the optimal working point to benefit from collective effects.

### C. Pareto optimal performances

Here, we generalize the analysis of the dissipation-induced collective effects on the performance of quantum thermal machine by (i) performing a functional optimization over arbitrary periodic driving

functions  $g_1^{(l)}(t)$  and (ii) deriving the Pareto front, i.e., the collection of driving functions that are Pareto-optimal tradeoffs between power and efficiency  $\eta = -P/J_1$ .<sup>89</sup> A Pareto-optimal cycle is one such that it is not possible to further improve the power or efficiency, without sacrificing the other one. The Pareto front is then defined as the collection of  $(\eta, -P)$  points of all Pareto-optimal cycles, which in general will include the maximum power case, the maximum efficiency case, and intermediate tradeoffs. Note that if a cycle is on the Pareto front of  $(\eta, -P)$ , it is also on the Pareto front of  $(\sigma, -P)$ , i.e., it is also Pareto-optimal between high power and low entropy production. Therefore, we search for the Pareto front in  $(\sigma, -P)$  and then transform these points to  $(\eta, -P)$  removing the non-Pareto-optimal ones. We determine the  $(\sigma, -P)$  Pareto front of the dynamical heat engine with respect to the driving coefficient  $g_n^{(l)}$  expressing both thermodynamic quantities as  $-P(\{g_n^{(l)}\})$  and  $\sigma(\{g_n^{(l)}\})$ . As shown in the supplementary material without loss of generality, we can assume the  $g_n^{(l)}$  coefficients to be real. We then consider a collection of fixed values of the entropy production rate  $\{\sigma_i\}$ , and for each one, we repeat the following optimization problem:

$$-P_i = \max_{\{g_n^{(l)}\}} \left[ -P(\{g_n^{(l)}\}) \right], \quad (21)$$

subject to  $\sigma(\{g_n^{(l)}\}) = \sigma_i$  and the two constraints in Eq. (10). The Pareto front is then given by all points  $\{(\sigma_i, -P_i)\}$ . Using Parseval's theorem, the two constraints in Eq. (10) are equivalent to bounding the time average of  $|g_1^{(l)}(t)|^2$ . This allows us to control the driving strength to both QHOs, ensuring that the coupling to bath 1 remains in the weak-coupling regime.

We solve the optimization problem in Eq. (21) numerically, using gradient-based optimization techniques, considering a set of 5000 discrete frequencies, i.e., 10 000 parameters  $g_n^{(l)}$  with  $n > 0$  [negative frequency coefficients must be the same as positive ones to guarantee that  $g^{(l)}(t)$  is real]. We then use automatic differentiation and the ADAM algorithm,<sup>90</sup> implemented in the PyTorch package,<sup>91</sup> to perform a gradient descent optimization starting from a random guess of the driving parameters. A modification of the Lagrange multipliers technique suitable for a gradient descent approach<sup>92</sup> is used to enforce the entropy constraint in Eq. (21), while the two constraints in Eq. (10) are exactly imposed renormalizing the coefficients (see the supplementary material for details). In Fig. 4, we report the results for the moderate damping case ( $\gamma_2 = 0.1\omega_A$ ) for three representative values of  $\omega_B$ . In all cases, the value of  $\omega_1$  has been chosen as the one that yields the maximum output power.

Notably, in all cases, the entire Pareto front of the bath-mediated situation in the joint case is strictly better than that of the independent configuration, i.e., for all points along the Pareto front of the independent case, there is at least one point in the joint case that yields higher power *and* higher efficiency. Furthermore, not only is the maximum power higher, but especially the efficiency of the joint case is enhanced along the entire Pareto front, reaching values that are twice as large in the  $\omega_B/\omega_A = 0.6, 0.9$  cases—see panels (c)–(f) of Fig. 4. Interestingly, as we move from  $\omega_B = 0.3\omega_A$  to  $\omega_B = 0.9\omega_A$ , the Pareto fronts move from a region of high power and low efficiency—upper left corner in panels (b), (d), and (f)—to a region of lower power but higher efficiency—lower right corner in panels (b), (d), and (f).

Again, the effect of the bath-mediated interaction between the QHOs is clearly visible, even in the moderate damping case,

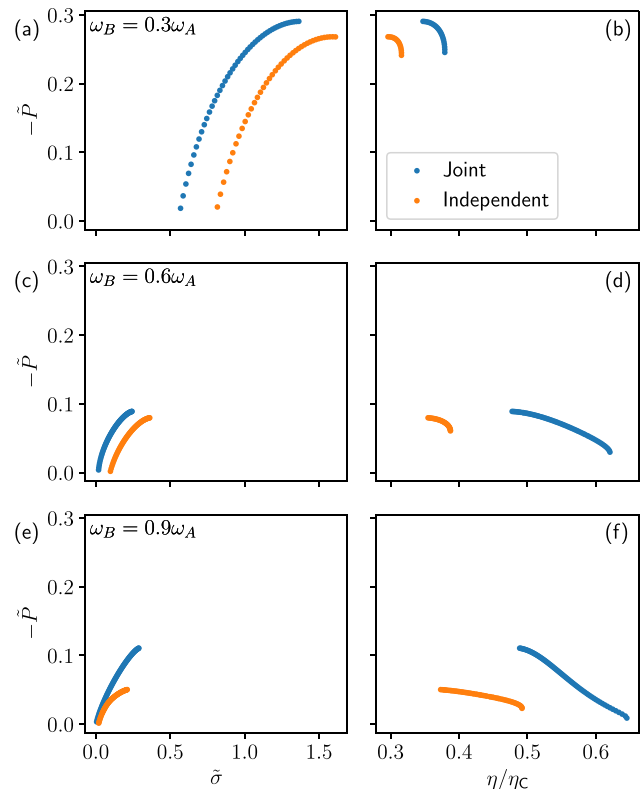


**Fig. 4.** Comparison between the joint (blue dots) and independent (orange dots) Pareto front in the moderate damping case, i.e.,  $\gamma_2 = 0.1\omega_A$ . The left column reports the Pareto front in the  $(\tilde{\sigma}, -\tilde{P})$  space, and the right column reports the same points in the  $(\eta/\eta_C, -\tilde{P})$ , where  $\eta_C = 1 - T_2/T_1$  is the Carnot efficiency. Each row corresponds to a different value of  $\omega_B/\omega_A$ : (a) and (b) correspond to 0.3, (c) and (d) 0.6, and (e) and (f) 0.9. For each  $\omega_B$ , the value of  $\omega_1$  is fixed to the one that yields maximum power as in Fig. 3(a). The driving magnitudes are fixed to  $|g^{(l)}|^2 \equiv \sum_n |g_n^{(l)}|^2 = 0.5$ , which are consistent with the monochromatic driving. All other system parameters are chosen as in Fig. 3. The numerical calculations are performed optimizing over 5000 evenly spaced frequencies, for each QHO, in the  $[0, 0.5\omega_A]$  interval. All plots report dimensionless quantities, i.e.,  $\tilde{P} = P\omega_A^2/d_1$  and  $\tilde{\sigma} = \sigma/\omega_A$ .

comparing the optimal driving in the joint and independent case. Indeed, in the latter, the optimal driving consists of applying two different frequencies to each QHO: intuitively, this is expected, since each QHO has a different characteristic frequency. However, in the joint case, the optimal driving turns out to be monochromatic along the entire Pareto front, for all explored values of  $\omega_B$  except for  $\omega_B = 0.6\omega_A$ , where two frequencies become optimal when the power is lower than  $|\tilde{P}| \sim 0.086$  (see the supplementary material).

In Fig. 5, we report the results of the joint case for the strong dissipation regime at  $\gamma_2/\omega_A = 100$ . As in Fig. 4, we set  $\omega_1$  to the value that yielded maximum power in the corresponding  $\omega_1 - \Omega$  plane and the left and right panels correspond, respectively, to the Pareto front in the  $(\sigma, -P)$  and  $(\eta, -P)$  space. The three curves correspond to the different values of  $\omega_B$  reported in the legend.

Remarkably, the strong dissipation regime displays a high-performance Pareto front, reaching values of the power that are roughly three times larger than in the moderate damping regime, while

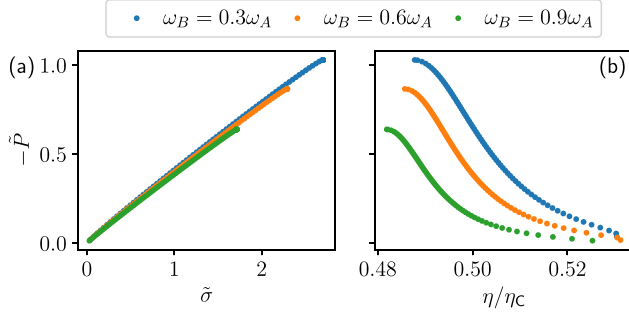


**Fig. 5.** Pareto front of the joint case in the ultra-strong damping regime, i.e.,  $\gamma_2 = 100\omega_A$ . As in Fig. 4, (a) reports the Pareto front in the  $(\hat{\sigma}, -P)$  space, and (b) reports the same points in the  $(\eta/\eta_C, -P)$ . Each curve corresponds to different values of  $\omega_B/\omega_A$  as shown in the legend. The driving magnitudes are fixed to  $|g^{(l)}|^2 = 0.5$ , which are consistent with the monochromatic driving. All other system parameters are chosen as in Fig. 3. The numerical calculations are performed optimizing over 5000 evenly spaced frequencies, for each QHO, in the  $[0, 0.5\omega_A]$  interval.

operating at a high efficiency  $\eta \sim 0.5\eta_C$ . In addition, the optimal driving along the entire Pareto front always consists of a monochromatic drive (see the supplementary material).

#### D. Measuring entanglement via average work

Before closing, we report another important result of the strong damping regime: we will demonstrate a direct prescription to assess the degree of entanglement for the WM from measurements of average works. The quantifier we use for detecting quantum correlations is the so-called logarithmic negativity<sup>35,42,66,67,69</sup>  $E_n$  (see the supplementary material). Here, we discuss a possible pathway to measure the degree of entanglement for a quantum system via thermodynamic observables.

We recall that the logarithmic negativity is defined as<sup>35,66,71</sup>

$$E_n \equiv \text{Max}[0, -\log(2\tilde{\nu})], \quad (22)$$

where  $\tilde{\nu}$  is the so-called symplectic eigenvalue of the partial transposed density matrix. Strictly positive values of  $E_n$  are a fingerprint of entanglement. To be in this regime,  $\tilde{\nu} < 1/2$  is required and this implies a constraint on temperatures: only for  $T < T_c$ , with  $T_c$  a critical temperature, the WM will be entangled. The behavior of  $T_c$  is shown in Fig. 6 as a function of  $\omega_B$  for different damping strengths  $\gamma_2$ . As one can see,  $T_c$  tends to saturate to the value  $T^*$  for  $\gamma_2 \rightarrow \infty$ . Since  $T^*$  is always the upper bound with respect to all other critical temperatures, we focus on the best working point at ultra-strong damping. In this regime, we found a closed analytic expression for  $\tilde{\nu}$  (see the supplementary material) given by

$$\tilde{\nu}^2 = \frac{\bar{\omega}^3 T_2 \coth^2\left(\frac{\bar{\omega}}{2T_2}\right)}{2(\bar{\omega}^4 - \Delta^4)} \frac{1}{\coth\left(\frac{\bar{\omega}}{2T_2}\right) + \frac{2T_2\Delta^4}{\bar{\omega}(\bar{\omega}^4 - \Delta^4)}}. \quad (23)$$

Using the above expression, we obtain the critical temperature  $T^*$  shown as a black curve in Fig. 6.

We will now demonstrate a direct link between  $\tilde{\nu}^2$  in Eq. (23) and a combination of works  $W$  [obtained from the average power as

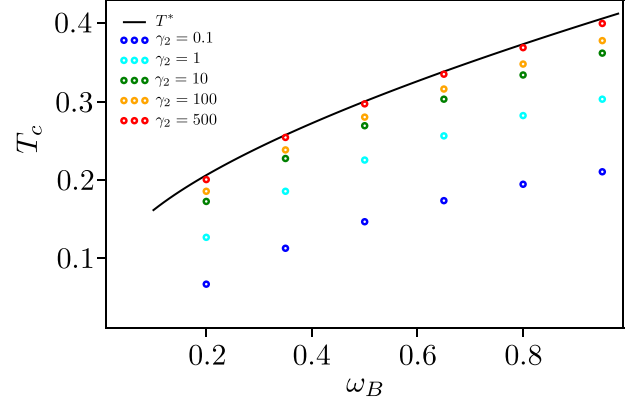


**Fig. 6.** Plot of the critical temperature  $T_c$  below which non-zero entanglement in the WM is expected as a function of  $\omega_B$  for different values of  $\gamma_2$  (see legend). The black solid line is the plot of the asymptotic critical temperature  $T^*$  for  $\gamma_2 \rightarrow \infty$ . All temperatures are in units of  $\omega_A$ .

$W = (2\pi/\Omega)P(\Omega)$ ] evaluated at different working points of the machine. As shown in the sketch of Fig. 7, we select three working points in the  $\omega_1 - \Omega$  plane, obtained at the intersection between the horizontal dotted line at a fixed  $\omega_1 = \omega_1^* < \bar{\omega}$  and three lines:  $\omega_1 = \bar{\omega} - \Omega$  (red),  $\omega_1 = \Omega$  (green), and  $\omega_1 = -\bar{\omega} + \Omega$  (blue). In addition, we consider a peaked spectral function  $\mathcal{J}_1(\omega)$ , acting as a sharp filter.

Using monochromatic drives, in the ultra-strong damping regime, the average work crucially depends on  $\phi$ . We now inspect the following combination of these average works:  $\Delta W_\phi = W_\phi^{(2)} + W_\phi^{(3)} - W_\phi^{(1)}$ . The result (see Appendix C) is

$$\Delta W_{\phi=\pi} = \frac{\pi}{m\bar{\omega}} \left[ \coth\left(\frac{\bar{\omega}}{2T_2}\right) + \frac{2T_2\Delta^4}{\bar{\omega}(\bar{\omega}^4 - \Delta^4)} \right] \mathcal{J}_1(\omega_1^*), \quad (24)$$

$$\Delta W_{\phi=0} = \frac{2\pi T_2}{m} \frac{\bar{\omega}^2}{\bar{\omega}^4 - \Delta^4} \mathcal{J}_1(\omega_1^*).$$

Comparing these results with  $\tilde{\nu}^2$  in Eq. (23), we arrive at the important identity

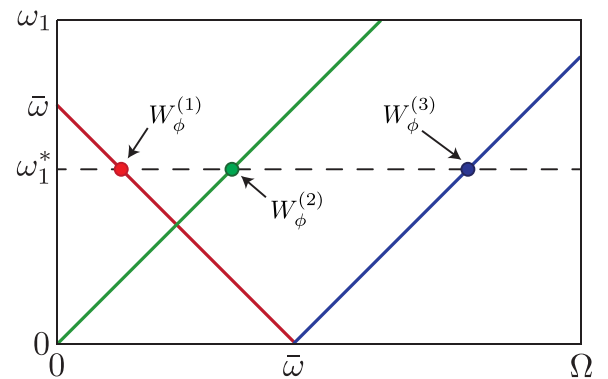


**Fig. 7.** Sketch of the three working points in the  $\omega_1 - \Omega$  plane where we evaluate the average work  $W_\phi^{(1,2,3)}$ . The horizontal dotted line highlights the representative value for  $\omega_1 = \omega_1^*$  around which the spectral density  $\mathcal{J}_1(\omega)$  is peaked.



$$\tilde{\nu}^2 = \frac{\coth^2\left(\frac{\bar{\omega}}{2T_2}\right)}{4} \frac{\Delta W_{\phi=0}}{\Delta W_{\phi=\pi}}. \quad (25)$$

This expression represents a direct link between entanglement and a function of the average works computed for specific driving protocols. Equation (25) is universal and does not depend on the particular working regime of the thermal machine, provided that ultra-strong damping has been reached.

#### IV. DISCUSSION

We have shown that dissipation can trigger a collective advantage for a quantum heat engine made of two non-interacting quantum harmonic oscillators connected to common heat baths, with the couplings to one of them periodically driven. This advantage is rooted in the non-trivial correlations between the oscillators mediated by the baths. Of particular interest is the regime of strong dissipation, where two independent single-oscillator engines working in parallel cannot deliver any power, whereas with common baths the engine shows high performances. The fact that the strong dissipation is a useful resource might seem surprising, but we have explained this result in terms of the appearance of a (weakly damped) frequency- and phase-locked mode, with the two oscillators moving with a common frequency and oscillating in phase opposition. The claim of collective advantage has been corroborated by the optimization over generic periodic driving protocols, building the full Pareto fronts and, thus, providing the optimal tradeoffs between power and efficiency. As a final outcome of our work, we have found a precise prescription in terms of thermodynamic quantities, such as average works, which allows to assess the degree of entanglement of the whole quantum system.

Our results open up several perspectives. First of all, it would be interesting to investigate whether the dissipation-induced collective advantage can be extended to  $N > 2$  oscillators and possibly to establish a link between collective advantage and multipartite quantum correlations. Second, it would be interesting to consider different, nonlinear working media, in particular hybrid oscillator-qubit systems of particular interest for quantum computing and more generally for quantum technologies. Third, our Pareto front analysis paves the way to the use of machine learning tools for non-Markovian quantum thermodynamics processes.

#### SUPPLEMENTARY MATERIAL

See the supplementary material for further technical details.

#### ACKNOWLEDGMENTS

M.C. and M.S. acknowledge support from the project PRIN 2022 - 2022PH852L (PE3) TopoFlags - “Non reciprocal supercurrent and topological transition in hybrid Nb-InSb nanoflags” funded within the programme “PNRR Missione 4 - Componente 2 - Investimento 1.1 Fondo per il Programma Nazionale di Ricerca e Progetti di Rilevante Interesse Nazionale (PRIN)”, funded by the European Union - Next Generation EU. L.R. and G.B. acknowledge financial support from the Julian Schwinger Foundation (Grant JSF-21-04-0001), from INFN through the project “QUANTUM”, and from the project PRIN 2022 - 2022XK5CPX (PE3) SoS-QuBa - “Solid State Quantum Batteries: Characterization and Optimization” funded within the programme “PNRR Missione 4 - Componente 2 - Investimento 1.1 Fondo per il Programma Nazionale di Ricerca e Progetti di Rilevante Interesse

Nazionale (PRIN)”, funded by the European Union - Next Generation EU. P. A. E. gratefully acknowledges funding by the Berlin Mathematics Center MATH+ (AA2-18).

#### AUTHOR DECLARATIONS

##### Conflict of Interest

The authors have no conflicts to disclose.

##### Author Contributions

**Matteo Carrega:** Investigation (equal); Methodology (equal); Writing – original draft (lead); Writing – review & editing (equal). **Luca Razzoli:** Investigation (equal); Software (equal); Writing – review & editing (equal). **Paolo Andrea Erdman:** Formal analysis (lead); Software (equal); Writing – original draft (supporting); Writing – review & editing (equal). **Fabio Cavaliere:** Investigation (equal); Software (equal); Writing – review & editing (equal). **Giuliano Benenti:** Conceptualization (equal); Supervision (equal); Writing – review & editing (equal). **Maura Sasseti:** Conceptualization (equal); Methodology (equal); Supervision (equal); Writing – review & editing (equal).

#### DATA AVAILABILITY

The data that support the findings of this study are available from the corresponding author upon reasonable request.

#### APPENDIX A: THERMODYNAMIC OBSERVABLES

The average power of Eq. (5) is associated with the time-dependent power operator, induced by the time varying coupling coefficients  $g_1^{(l)}(t)$  that modulate the  $\nu=1$  WM/bath coupling. Its expression is

$$P(t) = \frac{\partial H_{\text{int},1}^{(t)}}{\partial t} = \sum_{l=A,B} \sum_{k=1}^{+\infty} \left[ -\dot{g}_1^{(l)}(t) c_{k,1} x_l(t) X_{k,1}(t) + g_1^{(l)}(t) \dot{g}_1^{(l)}(t) \frac{c_{k,1}^2}{m_{k,1} \omega_{k,1}^2} x_l^2(t) + \partial_t \left[ g_1^{(l)}(t) g_1^{(l)}(t) \right] \times \frac{c_{k,1}^2}{2m_{k,1} \omega_{k,1}^2} x_l(t) x_l(t) \right]. \quad (A1)$$

The average heat currents in Eq. (6) instead describe the heat flows from or toward the  $\nu$ th reservoirs and depend on the operators  $J_\nu(t)$  given by

$$J_\nu(t) = -\dot{H}_\nu(t) = - \sum_{l=A,B} g_\nu^{(l)}(t) x_l(t) \sum_{k=1}^{+\infty} c_{k,\nu} \dot{X}_{k,\nu}(t). \quad (A2)$$

It is clear that these quantities depend on the WM and baths position operators, which obey a set of coupled equations of motion (see the supplementary material). The bath position operators can be expressed exactly as

$$X_{k,\nu}(t) = \xi_{k,\nu}(t) + \sum_{l=A,B} \frac{c_{k,\nu}}{m_{k,\nu} \omega_{k,\nu}} \int_{t_0}^t ds g_\nu^{(l)}(s) x_l(s) \sin[\omega_{k,\nu}(t-s)], \quad (A3)$$

where

$$\xi_{k,\nu}(t) \equiv X_{k,\nu}(t_0) \cos[\omega_{k,\nu}(t - t_0)] + \frac{P_{k,\nu}(t_0)}{m_{k,\nu}\omega_{k,\nu}} \sin[\omega_{k,\nu}(t - t_0)]. \quad (\text{A4})$$

The corresponding fluctuating force is

$$\xi_\nu(t) \equiv \sum_{k,\nu}^{+\infty} c_{k,\nu} \xi_{k,\nu}(t) \quad (\text{A5})$$

with zero quantum average  $\langle \xi_\nu(t) \rangle = 0$  and correlator<sup>74</sup>

$$\langle \xi_\nu(t) \xi_\nu(t') \rangle = \delta_{\nu,\nu'} \int_0^\infty \frac{d\omega}{\pi} \mathcal{J}_\nu(\omega) \times \left[ \coth\left(\frac{\omega}{2T_\nu}\right) \cos[\omega(t - t')] - i \sin[\omega(t - t')] \right]. \quad (\text{A6})$$

Looking at Eqs. (A1)–(A3), the behavior of these thermodynamic quantities is determined by the dynamics of  $x_A(t)$  and  $x_B(t)$ .

## APPENDIX B: TIME EVOLUTION OF QHO OPERATORS AND RESPONSE FUNCTIONS

The WM is weakly coupled to the  $\nu = 1$  reservoir. Therefore, in the main text, we have considered a perturbative expansion under which the position operator of the  $l$ th QHO can be then written as

$$x_l(t) = x_l^{(0)}(t) + \Delta x_l(t), \quad (\text{B1})$$

where  $x_l^{(0)}(t)$  evolves under the unperturbed Hamiltonian and is influenced only by the coupling with the static reservoir  $\nu = 2$ . The perturbative correction due to  $H_{\text{int},1}^{(1)}$  is (see the supplementary material)

$$\Delta x_l(t) = -i \sum_{\nu=A,B} \int_{t_0}^t ds g_1^{(\nu)}(s) \xi_1(s) [x_l^{(0)}(s), x_l^{(0)}(t)] \quad (\text{B2})$$

with  $\xi_1(t)$  defined in Eq. (A5). From this expression, it is clear that to evaluate Eqs. (5) and (6) via Eqs. (A1) and (A2), one needs the fluctuating force correlators<sup>74</sup>  $\langle \xi_1(t) \xi_1(t') \rangle$ , given in Eq. (A6), and  $\langle x_l^{(0)}(t) x_l^{(0)}(t') \rangle$ , which depends only on the static (unperturbed) bath  $\nu = 2$ . The latter are needed to evaluate the response functions  $\chi_2^{(l)}(t)$  defined in Eq. (11). To obtain its expression and study its properties, we begin considering the coordinates  $x_l^{(0)}(t)$  of the WM, which satisfy a set of coupled Langevin equations (see also the supplementary material). These equations can be conveniently written in Fourier space

$$\begin{aligned} [-\omega^2 + \omega_A^2 - i\omega\gamma_2(\omega)] x_A^{(0)}(\omega) - i\omega\gamma_2(\omega) x_B^{(0)}(\omega) &= \frac{\xi_2(\omega)}{m}, \\ [-\omega^2 + \omega_B^2 - i\omega\gamma_2(\omega)] x_B^{(0)}(\omega) - i\omega\gamma_2(\omega) x_A^{(0)}(\omega) &= \frac{\xi_2(\omega)}{m}. \end{aligned} \quad (\text{B3})$$

They depend on the noise term  $\xi_2(\omega) = \int_{-\infty}^\infty dt e^{i\omega t} \xi_2(t)$  with  $\xi_2(t)$  in Eq. (A5) and on the damping kernel in Fourier space  $\gamma_2(\omega)$ , defined in terms of the time kernel  $\gamma_2(t)$  (see the supplementary material) as

$$\gamma_2(\omega) = \int_{-\infty}^{+\infty} dt e^{i\omega t} \theta(t) \gamma_2(t). \quad (\text{B4})$$

To understand the physics of two QHOs with bath-mediated interactions, we study in Eq. (B3) the intrinsic excitations of the normal modes in the absence of the noise term [i.e., setting  $\xi_2(\omega) = 0$ ]. Following the standard procedure,<sup>74</sup> they are given by the zeros of  $D(\omega)$  in Eq. (13), which is the determinant of the coefficient matrix of Eq. (B3). These zeros, which are four in our case:  $z_j = z_j' + iz_j''$ , determine the dynamics of  $x_{A,B}^{(0)}(t)$  at finite times. In particular, their real parts give the possible frequencies of oscillations, while the imaginary ones describe their damping. Their explicit form will depend on the shape of the damping kernel  $\gamma_2(\omega)$  and, eventually, on the spectral density of the static bath  $\nu = 2$ . Here, we consider a Ohmic spectral density with a Drude cut-off  $\mathcal{J}_2(\omega) = m\omega\gamma_2 / (1 + \omega^2/\omega_c^2)$ , which leads to  $\gamma_2'(\omega) = \mathcal{J}_2(\omega)/m\omega$  and  $\gamma_2''(\omega) = \mathcal{J}_2(\omega)/m\omega_c$ <sup>74</sup> with  $\omega_c$  the high energy cutoff. When not necessary, we will consider the latter as the highest energy of the system ( $\omega_c \rightarrow \infty$ ) with then  $\mathcal{J}_2(\omega) = m\omega\gamma_2$ , and a constant and real  $\gamma_2(\omega) = \gamma_2$ .

In Fig. 8, we report the real—panel (a)—and imaginary—panel (b)—parts of the four zeros as a function of the damping strength  $\gamma_2$ . Looking at Fig. 8(a), it is easy to see that for  $\gamma_2 \ll \omega_{A,B}$ , the system behaves as two independent QHOs with characteristic frequencies  $\omega_A$  and  $\omega_B$ . On the other hand, at large damping  $\gamma_2 \gg \Delta^4/\bar{\omega}^3$  [with  $\bar{\omega}$  in Eq. (15) and  $\Delta^2 = (\omega_A^2 - \omega_B^2)/2$ ] two modes are frequency locked to the common frequency  $\bar{\omega}$ , with  $z_1' = -z_4' \rightarrow \bar{\omega}$ , while the other two are overdamped, namely,  $z_2' = -z_3' = 0$ .

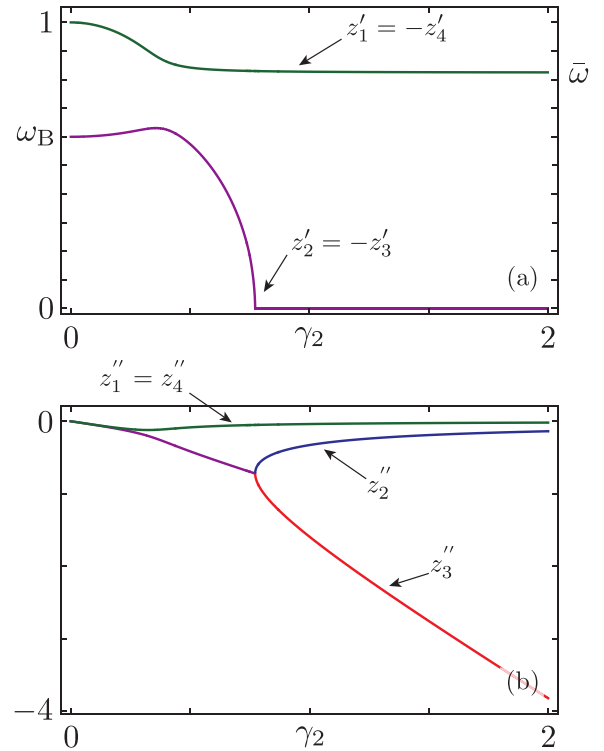


**Fig. 8.** Plot of (a) the real part  $z_j'$  and (b) the imaginary part  $z_j''$  of the four zeros of  $D(\omega)$  for the case of a Ohmic spectral density for the  $\nu = 2$  bath in the limit of large cut-off  $\omega_c \rightarrow \infty$ , as a function of the damping strength  $\gamma_2$  for representative parameter values  $\omega_A = 1$  and  $\omega_B = 0.6$ . All quantities are in units of  $\omega_A$ .

Considering now the imaginary parts shown in Fig. 8(b), we see that for small damping, they all are  $\propto \gamma_2$  and acquire different behaviors at larger  $\gamma_2$ . In particular, the zeros that tend to a finite frequency  $z'_1 = -z'_4 \rightarrow \bar{\omega}$  have imaginary parts that tend to vanish with increasing  $\gamma_2$ . On the other hand, the overdamped ones  $z_2$  and  $z_3$  possess imaginary contributions that run together until a critical value and bifurcate after it with opposite behavior.

In the regime of very weak  $\gamma_2 \ll \omega_{A,B}$ , we obtain

$$z_{1,4} = \pm \omega_A - i \frac{\gamma_2}{2}; \quad z_{2,3} = \pm \omega_B - i \frac{\gamma_2}{2}, \quad (B5)$$

while at ultra-strong damping  $\gamma_2 \gg \Delta^4/\bar{\omega}^3$ , we have

$$z_{1,4} = \pm \bar{\omega} - i \frac{\Delta^4}{4\gamma_2 \bar{\omega}^2}; \quad z_2 = -i \frac{(\bar{\omega}^4 - \Delta^4)}{2\gamma_2 \bar{\omega}^2}; \quad z_3 = -2i\gamma_2, \quad (B6)$$

in full agreement with the behavior reported in Fig. 8. Notice that the zeros that survive at the common frequency  $\bar{\omega}$  are very stable, i.e., with a very small imaginary part  $\propto 1/\gamma_2$ .

The aforementioned results demonstrate that at strong damping, the two QHOs become *frequency locked* oscillating, at finite time, with a common frequency  $\bar{\omega}$ . Moreover, they are also *phase locked* in anti-phase (with relative phase  $\pi$ ), as one can see from the relation of the homogeneous solution of Eq. (B3) with  $x_A(\omega) = -x_B(\omega)$  at large  $\gamma_2$ . All these regimes are reflected on the retarded response function. Indeed, switching on the noise  $\xi_2(\omega)$ , the system (B3) has the long time compact solution  $\mathbf{x}^\dagger = \chi_2 \cdot \xi^\dagger/m$ , where  $\mathbf{x} = (x_A^{(0)}(\omega), x_B^{(0)}(\omega))$  is the two-component vector of the positions of the oscillators,  $\xi = \xi_2(\omega)(1, 1)$  is the noise vector, and  $\chi_2(\omega)$  is the two-by-two response-function matrix, inverse of the coefficient matrix. Its elements are the Fourier transform of Eq. (11) and are given by

$$\chi_2^{(ll)}(\omega) = \frac{-[\omega^2 - \omega_l^2 + i\omega\gamma_2(\omega)]}{D(\omega)}; \quad \chi_2^{(ll)}(\omega) = \frac{i\omega\gamma_2(\omega)}{D(\omega)}. \quad (B7)$$

The behavior of the response function is connected to the already discussed normal modes. We are particularly interested in the imaginary part of such response function.

At very weak damping ( $\gamma_2 \ll \omega_{A,B}$ ),  $\chi_2''(\omega)$  is exactly the one of two independent QHOs [see also Eq. (B5)],

$$\chi_2^{(ll)''}(\omega) = \delta_{l,l'} \frac{i\omega\gamma_2}{(\omega^2 - \omega_l^2)^2 + \omega^2\gamma_2^2}. \quad (B8)$$

In the opposite regime ( $\gamma_2 \gg \Delta^4/\bar{\omega}^3$ ) from Eq. (B6), we obtain

$$\chi_2^{(ll)''}(\omega) = \left[ (1 - \delta_{l,l'}) + \frac{\omega_l^2}{\omega_l^2} \delta_{l,l'} \right] \frac{\omega}{\omega_l^2 + \omega_l^2 \omega^2 + |z_l''|^2} + \frac{\omega(-1)^{1-\delta_{l,l'}}}{2(\omega_l^2 + \omega_l^2)} \sum_{p=\pm} \frac{|z_1''|}{\left( \omega + p\sqrt{(\omega_l^2 + \omega_l^2)/2} \right)^2 + |z_1''|^2}. \quad (B9)$$

Here, since  $z_1''$  and  $z_2''$  scale as  $1/\gamma_2$ —see Eq. (B6)—both the diagonal and the off diagonal response functions are dominated by contributions peaked around  $\pm \bar{\omega} = \pm \sqrt{(\omega_A^2 + \omega_B^2)/2}$ . Indeed in this regime, the WM becomes effectively *frequency locked* to a unique

common frequency, i.e.,  $\bar{\omega}$ . In addition, the phase locking at  $\pi$ , discussed above, is here reflected in the property  $\chi_2^{(ll)''}(\omega) \rightarrow -\chi_2^{(ll)''}(\omega)$ . Note that the first term in Eq. (B9)  $\propto \omega$ , although negligible with respect to the second one, can give a finite dissipative contributions to the power (see below).

For the sake of comparison, we quote the behavior associated with the independent configuration [see Fig. 1(b)]. In this case, the response function is diagonal and given by  $\chi_{2,\text{ind}}^{(ll)''}(\omega) = -\delta_{l,l'}/[\omega^2 - \omega_l^2 + i\omega\gamma_2]$ . It is then straightforward to see that at very weak damping, the normal modes are the same as in the joint case in Eq. (B5), while for strong damping, they are given by  $z_{1,\text{ind}} = -i\omega_A^2/\gamma_2$ ,  $z_{2,\text{ind}} = -i\omega_B^2/\gamma_2$  and  $z_{3,4,\text{ind}} = -i\gamma_2$ . As we can see, in the latter case, all zeros are purely imaginary, implying always an overdamped regime at strong damping. This behavior is in sharp contrast with the case discussed above of the joint configuration.

### APPENDIX C: AVERAGE POWER FOR WEAK AND STRONG DAMPING

To obtain expressions for the average power  $P$  in the weak and in the strong damping regime, we start from Eq. (19) and the expressions for  $\chi_2^{(ll)''}(\omega)$  quoted above.

In the very weak damping regime  $\gamma_2 \ll \omega_{A,B}$ , the average power is phase-independent, and using Eq. (B8), we get

$$P = -\frac{\Omega}{8m} \sum_{l=A,B} \frac{1}{\omega_l} \sum_{p=\pm} p \mathcal{J}_1(p\omega_l + \Omega) N(p\omega_l, \Omega). \quad (C1)$$

In the opposite regime of ultra-strong damping  $\gamma_2 \gg \Delta^4/\bar{\omega}^3$ , we use instead Eq. (B9). Here, the power depends on the phase  $\phi$ . When  $\phi = \pi$ , one finds

$$P_\pi = \frac{\Omega}{4m\bar{\omega}} \left[ \frac{T_2(\omega_B^2 - \omega_A^2)^2}{\bar{\omega}\omega_A^2\omega_B^2} \mathcal{J}_1(\Omega) - \sum_{p=\pm} p \mathcal{J}_1(p\bar{\omega} + \Omega) N(p\bar{\omega}, \Omega) \right], \quad (C2)$$

while for the case  $\phi = 0$  the dominant contributions of  $\chi_2^{(ll)''}(\omega)$ , around the characteristic frequency  $\bar{\omega}$ , cancels out in  $\chi_{\text{eff}}(\omega)$  and only the dissipative part around  $\omega \sim 0$  remains yielding

$$P_0 = \frac{\Omega}{2m} T_2 \mathcal{J}_1(\Omega) \left( \frac{1}{\omega_A^2} + \frac{1}{\omega_B^2} \right) > 0, \quad (C3)$$

i.e., no useful power can be delivered. Importantly, we notice that the corresponding power of the independent case,  $P_{\text{ind}}$ , coincides exactly with the above result:  $P_{\text{ind}} \equiv P_0$ . Indeed, in this regime, we have  $\chi_{\text{eff}}^{\text{ind}}(\omega) = \sum_{l=A,B} i/[\gamma_2(\omega + i\omega_l^2/\gamma_2)]$ .

From the above equations, it is easy to obtain the analytic expressions of the average work at ultra-strong damping along the lines of Fig. 7. For  $\phi = \pi$ , we have

$$\begin{aligned} W_{\phi=\pi}^{(1)} &= -\frac{\pi}{2m\bar{\omega}} \mathcal{J}_1(\omega_1^*) N(-\bar{\omega}, \bar{\omega} - \omega_1^*), \\ W_{\phi=\pi}^{(2)} &= \frac{\pi}{2m\bar{\omega}^2} \frac{T_2(\omega_B^2 - \omega_A^2)^2}{\omega_A^2\omega_B^2} \mathcal{J}_1(\omega_1^*), \\ W_{\phi=\pi}^{(3)} &= \frac{\pi}{2m\bar{\omega}} \mathcal{J}_1(\omega_1^*) N(-\bar{\omega}, \bar{\omega} + \omega_1^*), \end{aligned} \quad (C4)$$

while for  $\phi = 0$ , we obtain

$$W_{\phi=0}^{(2)} = \frac{\pi T_2}{m} \left( \frac{1}{\omega_A^2} + \frac{1}{\omega_B^2} \right) \mathcal{J}_1(\omega_1^*), \quad (\text{C5})$$

and  $W_{\phi=0}^{(1)}, W_{\phi=0}^{(3)} \rightarrow 0$ . From the above expressions, it is immediate to obtain the expressions for  $\Delta W_\phi$  quoted in Eq. (24).

## REFERENCES

- <sup>1</sup>A. Acin *et al.*, *New J. Phys.* **20**, 080201 (2018).
- <sup>2</sup>G. Benenti, G. Casati, D. Rossini, and G. Strini, *Principles of Quantum Computation and Information* (World Scientific, Singapore, 2019).
- <sup>3</sup>R. Kosloff, *Entropy* **15**, 2100 (2013).
- <sup>4</sup>D. Gelbwaser-Klimovsky, W. Niedenzu, and G. Kurizki, "Thermodynamics of quantum systems under dynamical control," in *Advances in Atomic, Molecular, and Optical Physics*, edited by E. Arimondo, C. C. Lin, and S. F. Yelin (Academic Press, 2015), Vol. 64, p. 329.
- <sup>5</sup>B. Sothmann, R. Sánchez, and A. N. Jordan, *Nanotechnology* **26**, 032001 (2015).
- <sup>6</sup>S. Vinjanampathy and J. Anders, *Contemp. Phys.* **57**, 545 (2016).
- <sup>7</sup>J. Goold, M. Huber, A. Riera, L. del Rio, and P. Skrzypczyk, *J. Phys. A* **49**, 143001 (2016).
- <sup>8</sup>G. Benenti, G. Casati, K. Saito, and R. S. Whitney, *Phys. Rep.* **694**, 1 (2017).
- <sup>9</sup>M. Wiedmann, J. T. Stockburger, and J. Ankerhold, *New J. Phys.* **22**, 033007 (2020).
- <sup>10</sup>G. T. Landi and M. Paternostro, *Rev. Mod. Phys.* **93**, 035008 (2021).
- <sup>11</sup>J. P. Pekola and B. Karimi, *Rev. Mod. Phys.* **93**, 041001 (2021).
- <sup>12</sup>L. Arrachea, *Rep. Prog. Phys.* **86**, 036501 (2023).
- <sup>13</sup>G. T. Landi, D. Poletti, and G. Schaller, *Rev. Mod. Phys.* **94**, 045006 (2022).
- <sup>14</sup>L. M. Cangemi, C. Bhadra, and A. Levy, "Quantum engines and refrigerators," [arXiv:2302.00726](https://arxiv.org/abs/2302.00726) (2023).
- <sup>15</sup>R. Lopez, J. S. Lim, and K. W. Kim, "An optimal superconducting hybrid machine," [arXiv:2209.09654](https://arxiv.org/abs/2209.09654) (2022).
- <sup>16</sup>R. Lopez, P. Simon, and M. Lee, "Heat and charge transport in interacting nanoconductors driven by time-modulated temperatures," [arXiv:2308.03426](https://arxiv.org/abs/2308.03426) (2023).
- <sup>17</sup>V. Sing, V. Shaghghi, T. Pandit, C. Beetar, G. Benenti, and D. Rosa, "The asymmetric Otto engine: frictional effects on performance bounds and operational modes," [arXiv:2310.06512](https://arxiv.org/abs/2310.06512) (2023).
- <sup>18</sup>L. Arrachea, E. R. Mucciolo, C. Chamon, and R. B. Capaz, *Phys. Rev. B* **86**, 125424 (2012).
- <sup>19</sup>L. M. Cangemi, M. Carrega, A. De Candia, V. Cataudella, G. De Filippis, M. Sasseti, and G. Benenti, *Phys. Rev. Res.* **3**, 013237 (2021).
- <sup>20</sup>M. Xu, J. T. Stockburger, G. Kurizki, and J. Ankerhold, *New J. Phys.* **24**, 035003 (2022).
- <sup>21</sup>M. Campisi and R. Fazio, *Nat. Commun.* **7**, 11895 (2016).
- <sup>22</sup>J. Jaramillo, M. Beau, and A. del Campo, *New J. Phys.* **18**, 075019 (2016).
- <sup>23</sup>H. Vroylandt, M. Esposito, and G. Verley, *Europhys. Lett.* **120**, 30009 (2018).
- <sup>24</sup>A. Ü. C. Hardal, M. Paternostro, and Ö. E. Müstecaplıoğlu, *Phys. Rev. E* **97**, 042127 (2018).
- <sup>25</sup>W. Niedenzu and G. Kurizki, *New J. Phys.* **20**, 113038 (2018).
- <sup>26</sup>D. Gelbwaser-Klimovsky, W. Kopylov, and G. Schaller, *Phys. Rev. A* **99**, 022129 (2019).
- <sup>27</sup>C. L. Latune, I. Sinayskiy, and F. Petruccione, *New J. Phys.* **22**, 083049 (2020).
- <sup>28</sup>G. Manzano, G. Giorgi, R. Fazio, and R. Zambrini, *New J. Phys.* **21**, 123026 (2019).
- <sup>29</sup>N. Jaseem, S. Vinjanampathy, and V. Mukherjee, *Phys. Rev. A* **107**, 40202 (2023).
- <sup>30</sup>G. Watanabe, B. P. Venkatesh, P. Talkner, M.-J. Hwang, and A. del Campo, *Phys. Rev. Lett.* **124**, 210603 (2020).
- <sup>31</sup>L. da Silva Souza, G. Manzano, R. Fazio, and F. Iemini, *Phys. Rev. E* **106**, 014143 (2022).
- <sup>32</sup>H. Tajima and K. Funo, *Phys. Rev. Lett.* **127**, 190604 (2021).
- <sup>33</sup>S. Kamimura, H. Hakoshima, Y. Matsuzaki, K. Yoshida, and Y. Tokura, *Phys. Rev. Lett.* **128**, 180602 (2022).
- <sup>34</sup>S. Kamimura, K. Yoshida, Y. Tokura, and Y. Matsuzaki, *Phys. Rev. Lett.* **131**, 090401 (2023).
- <sup>35</sup>J. P. Paz and A. J. Roncaglia, *Phys. Rev. A* **79**, 032102 (2009).
- <sup>36</sup>F. Galve, G. L. Giorgi, and R. Zambrini, *Phys. Rev. A* **81**, 062117 (2010).
- <sup>37</sup>L. A. Correa, A. A. Valido, and D. Alonso, *Phys. Rev. A* **86**, 012110 (2012).
- <sup>38</sup>O. S. Duarte and A. O. Caldeira, *Phys. Rev. Lett.* **97**, 250601 (2006).
- <sup>39</sup>L. Henriot, *Phys. Rev. A* **100**, 022119 (2019).
- <sup>40</sup>L. A. Correa, J. P. Palao, G. Adesso, and D. Alonso, *Phys. Rev. E* **87**, 042131 (2013).
- <sup>41</sup>A. A. Valido, A. Ruiz, and D. Alonso, *Phys. Rev. E* **91**, 062123 (2015).
- <sup>42</sup>C. Henkel, *Ann. Phys.* **533**, 2100089 (2021).
- <sup>43</sup>C. G. Feyisa and H. H. Jen, "A photonic engine fueled by quantum-correlated atoms," [arXiv:2307.16726](https://arxiv.org/abs/2307.16726) (2023).
- <sup>44</sup>X. Li, J. Marino, D. E. Chang, and B. Flebus, "A solid-state platform for cooperative quantum phenomena," [arXiv:2309.08991](https://arxiv.org/abs/2309.08991) (2023).
- <sup>45</sup>A. Rolandi and M. Perarnau-Llobet, "Collective advantages in finite-time thermodynamics," [arXiv:2306.16534](https://arxiv.org/abs/2306.16534) (2023).
- <sup>46</sup>A. C. Hardal and O. Mustecaplıoğlu, *Sci. Rep.* **5**, 12953 (2015).
- <sup>47</sup>M. Carrega, L. M. Cangemi, G. De Filippis, V. Cataudella, G. Benenti, and M. Sasseti, *PRX Quantum* **3**, 010323 (2022).
- <sup>48</sup>F. Cavaliere, M. Carrega, G. De Filippis, V. Cataudella, G. Benenti, and M. Sasseti, *Phys. Rev. Res.* **4**, 033233 (2022).
- <sup>49</sup>F. Cavaliere, L. Razzoli, M. Carrega, G. Benenti, and M. Sasseti, *iScience* **26**, 106235 (2023).
- <sup>50</sup>G. L. Giorgi, F. Galve, G. Manzano, P. Colet, and R. Zambrini, *Phys. Rev. A* **85**, 052101 (2012).
- <sup>51</sup>G. Manzano, F. Galve, G. L. Giorgi, E. Hernández-García, and R. Zambrini, *Sci. Rep.* **3**, 1439 (2013).
- <sup>52</sup>L. Du, C.-H. Fan, H.-X. Zhang, and J.-H. We, *Sci. Rep.* **7**, 15834 (2017).
- <sup>53</sup>H. Geng, L. Du, H. D. Liu, and X. X. Yi, *J. Phys. Commun.* **2**, 025032 (2018).
- <sup>54</sup>Y. Ashida and T. Sagawa, *Commun. Phys.* **4**, 45 (2021).
- <sup>55</sup>P. Abiuso and M. Perarnau-Llobet, *Phys. Rev. Lett.* **124**, 110606 (2020).
- <sup>56</sup>P. Abiuso, H. J. D. Miller, M. Perarnau-Llobet, and M. Scandi, *Entropy* **22**, 1076 (2020).
- <sup>57</sup>P. A. Erdman, A. Rolandi, P. Abiuso, M. Perarnau-Llobet, and F. Noé, *Phys. Rev. Res.* **5**, L022017 (2023).
- <sup>58</sup>P. A. Erdman and F. Noé, *PNAS Nexus* **2**, pgad248 (2023).
- <sup>59</sup>P. Sgroi, G. M. Palma, and M. Paternostro, *Phys. Rev. Lett.* **126**, 020601 (2021).
- <sup>60</sup>P. A. Erdman and F. Noé, *npj Quantum Inf.* **8**, 1 (2022).
- <sup>61</sup>I. Khaït, J. Carrasquilla, and D. Segal, *Phys. Rev. Res.* **4**, L012029 (2022).
- <sup>62</sup>V. Pareto, *Manuale di Economia Politica* (Società Editrice Libreria, Milan, 1906) , [*Manual of Political Economy* (Oxford University Press, Oxford, 2014) (in English)].
- <sup>63</sup>V. Patel, V. Savsani, and A. Mudgal, *Energy* **125**, 629 (2017).
- <sup>64</sup>A. P. Solon and J. M. Horowitz, *Phys. Rev. Lett.* **120**, 180605 (2018).
- <sup>65</sup>J. Gonzalez-Ayala, J. Guo, A. Medina, J. M. M. Roco, and A. Calvo Hernández, *Phys. Rev. Lett.* **124**, 050603 (2020).
- <sup>66</sup>R. Simon, *Phys. Rev. Lett.* **84**, 2726 (2000).
- <sup>67</sup>A. Serafini, F. Illuminati, M. G. A. Paris, and S. De Siena, *Phys. Rev. A* **69**, 022318 (2004).
- <sup>68</sup>J. P. Paz and A. J. Roncaglia, *Phys. Rev. Lett.* **100**, 220401 (2008).
- <sup>69</sup>R. Schmidt, J. T. Stockburger, and J. Ankerhold, *Phys. Rev. A* **88**, 052321 (2013).
- <sup>70</sup>G. Vidal and R. F. Werner, *Phys. Rev. A* **65**, 032314 (2002).
- <sup>71</sup>M. B. Plenio, *Phys. Rev. Lett.* **95**, 090503 (2005).
- <sup>72</sup>The superscript <sup>(t)</sup> reminds the time-dependent modulation  $g_1^{(t)}(t)$ .
- <sup>73</sup>A. O. Caldeira and A. J. Leggett, *Ann. Phys.* **149**, 374 (1983).
- <sup>74</sup>U. Weiss, *Quantum Dissipative Systems*, 5th ed. (World Scientific, Singapore, 2021).
- <sup>75</sup>U. Weiss, R. Egger, and M. Sasseti, *Phys. Rev. B* **52**, 16707 (1995).
- <sup>76</sup>E. Aurell, *Phys. Rev. E* **97**, 062117 (2018).
- <sup>77</sup>M. Esposito, K. Lindenberg, and C. Van den Broeck, *New J. Phys.* **12**, 013103 (2010).
- <sup>78</sup>M. Thorwart, E. Paladino, and M. Grifoni, *Chem. Phys.* **296**, 333 (2004).
- <sup>79</sup>E. Paladino, A. G. Mauger, M. Sasseti, G. Falci, and U. Weiss, *Physica E* **40**, 198 (2007).
- <sup>80</sup>J. Iles-Smith, N. Lambert, and A. Nazir, *Phys. Rev. A* **90**, 032114 (2014).
- <sup>81</sup>S. Gröblacher, A. Trubarov, N. Prigge, G. D. Cole, M. Aspelmeyer, and J. Eisert, *Nat. Commun.* **6**, 7606 (2015).

<sup>82</sup>G. Torre, W. Roga, and F. Illuminati, *Phys. Rev. Lett.* **115**, 070401 (2015).

<sup>83</sup>Note that in the case of a strictly Ohmic spectral function  $\mathcal{J}_1(\omega) = m\gamma_1\omega$  no working heat engine regime is expected.<sup>48</sup>

<sup>84</sup>A. Cottet, M. C. Dartiailh, M. M. Desjardins, T. Cubaynes, L. C. Contamin, M. Delbecq, J. J. Viennot, L. E. Bruhat, B. Douçot *et al.*, *J. Phys.: Condens. Matter* **29**, 433002 (2017).

<sup>85</sup>A. Calzona and M. Carrega, *Supercond. Sci. Technol.* **36**, 023001 (2023).

<sup>86</sup>B. Peropadre, D. Zueco, F. Wulshner, F. Deppe, A. Marx, R. Gross, and J. J. García-Ripoll, *Phys. Rev. B* **87**, 134504 (2013).

<sup>87</sup>I. C. Rodrigues, D. Bothner, and G. A. Steele, *Nat. Commun.* **10**, 5359 (2019).

<sup>88</sup>We have investigated other temperature configurations in the engine working mode and no qualitative changes have been observed. Furthermore, we underline that higher values of  $\gamma_1$  than the other reported would produce smaller

output power magnitudes, with no qualitative changes for the collective advantage.

<sup>89</sup>L. F. Seoane and R. Solé, “Multiobjective optimization and phase transitions,” in *Proceedings of ECCS*, edited by S. Battiston, F. De Pellegrini, G. Caldarelli, and E. Merelli (Springer, Cham, 2016).

<sup>90</sup>D. P. Kingma and J. Ba, “Adam: A method for stochastic optimization,” [arXiv:1412.6980](https://arxiv.org/abs/1412.6980) (2017).

<sup>91</sup>A. Paszke *et al.*, “PyTorch: An imperative style, high-performance deep learning library,” in *Advances in Neural Information Processing Systems 32*, edited by H. Wallach, H. Larochelle, A. Beygelzimer, F. d’Alché-Buc, E. Fox, and R. Garnett (NeurIPS, 2019).

<sup>92</sup>J. C. Platt and A. H. Barr, “Constrained differential optimization,” in *Neural Information Processing Systems 0*, edited by D. Anderson (American Institute of Physics, 1987), p. 612.